Deep–Sea Research I 197 (2023) 104041

Contents lists available at ScienceDirect

Deep-Sea Research Part I

journal homepage: www.elsevier.com/locate/dsri

Mechanisms for generating and connecting the Yanai-mode and Rossby-mode tropical instability waves in the equatorial Pacific

Wei-Bang He[a], Yang Yang[b], X. San Liang[c,d,e,*]

[a] School of Marine Sciences, Nanjing University of Information Science and Technology, Nanjing, China
[b] State Key Laboratory of Marine Environmental Science, and Department of Physical Oceanography, College of Ocean and Earth Sciences, Xiamen University, Xiamen, China
[c] Department of Atmospheric and Oceanic Sciences, and Institute of Atmospheric Sciences, Fudan University, Shanghai, China
[d] IRDR ICoE on Risk Interconnectivity and Governance on Weather/Climate Extremes Impact and Public Health, Fudan University, Shanghai, China
[e] The Artificial Intelligence Group, Division of Frontier Research, Southern Marine Laboratory, Zhuhai, China

ARTICLE INFO

Keywords:
Tropical instability waves
Yanai wave
Equatorial Pacific Ocean
Multiscale window transform
Canonical transfer

ABSTRACT

It is generally believed that both barotropic and baroclinic instabilities may account for the tropical instability wave (TIW) variabilities in the equatorial Pacific Ocean. However, the coupling mechanisms between the two different meridional TIW modes, i.e., the Yanai-mode at the equator and the Rossby-mode around 5°N, and the associated vertical connections, are yet to be clarified. This is done here using a recently developed multiscale decomposition tool, multiscale window transform (MWT), and the MWT-based theory of canonical transfer and TIW-scale eddy kinetic energy (EKE) budget analysis, based on the $(1/12.5)^\circ$ HYCOM reanalysis data. In the subsurface layer (30–200 m), barotropic instability is the primary energy source for the Yanai-mode TIWs, while baroclinic instability dominates the EKE generation of the Rossby-mode TIWs. In contrast, the two TIW modes in the surface layer (0–30 m) are largely modulated by nonlocal mechanisms through pressure work, which functions to transport EKE upward from the subsurface to the surface layer, and southward from the Rossby-mode region to the Yanai-mode region. The pressure fluxes substantially couple the two TIW modes in both the meridional and vertical directions, leading to significant coherence between EKE in different vertical layers and regions of the TIWs. In addition, the prevailing vertical pressure flux identified north of the equator explains why the EKE signal is more vertically coherent in the Rossby-mode region than the Yanai-mode region. This nonlocal energy pathway, as well as the well-known instability processes, undergoes strong seasonal variations that determine the seasonal cycles of the TIWs in the equatorial Pacific Ocean.

1. Introduction

Tropical Instability Waves (TIWs) are the dominant mesoscale variability in the eastern equatorial Pacific Ocean. In satellite images, TIWs are visible as westward propagating wave trains with well-organized, cusp-shaped anti-cyclonic structures riding on the sea surface temperature (SST) fronts of the equatorial cold tongue (Legeckis 1977). TIWs propagate with a phase velocity of about 0.5 m/s and a wavelength of 1000–2000 km (Legeckis 1977; Philander 1978; Weisberg and Weingartner 1988; Qiao and Weisberg 1995; Chelton and Coauthors, 2001; Contreras 2002). They can induce 1–2 °C perturbation of SST and intense heat flux in the upper ocean, which may modulate the asymmetry of the El Niño–Southern Oscillation (ENSO) (Vialard et al., 2001; An 2008; Kimoto and Imada 2012; Holmes and Thomas 2016; Xue et al., 2020).

TIWs have been suggested to be categorized into two modes. The first mode is characterized by strong variability of meridional velocity with periods of around 17.5 days near the equator, resembling the Yanai waves and inducing northeast-southwest velocity oscillations centered at the equator (Halpern et al., 1988; Bryden and Brady 1989; Qiao and Weisberg 1995; Lyman et al., 2007; Liu et al., 2019b). The second mode, which is centered at ∼ 5°N, has periods of around 33 days and is characterized by anticyclonic vortices known as Tropical Instability Vortices (TIVs) with warm edges along the equator and cold cusps to the north. The 33-day TIWs resemble Rossby waves, inducing northwest–southeastward velocity oscillations around 5°N (Flament et al., 1996; Kennan and Flament 2000; Lyman et al., 2007; Wang et al., 2020). For simplicity, the two dominant TIW modes occurring in these two distinct

---

[*] Corresponding author. Department of Atmospheric and Oceanic Sciences, and Institute of Atmospheric Sciences, Fudan University, Shanghai, China.
E-mail address: xsliang@fudan.edu.cn (X.S. Liang).

https://doi.org/10.1016/j.dsr.2023.104041
Received 19 November 2022; Received in revised form 25 March 2023; Accepted 2 April 2023

regions are respectively referred to as Yanai-mode and Rossby-mode in this study.

A rich literature exists addressing the generation mechanisms of the TIWs. It is generally believed that TIWs are generated by mixed barotropic and baroclinic instabilities. Strong meridional velocity shear between the northern branch of the South Equatorial Current (SEC), the North Equatorial Countercurrent (NECC), and the Equatorial Undercurrent (EUC) provides favorable conditions for barotropic instability that trigger the TIWs (Philander 1976, 1978; Cox 1980; Luther and Johnson 1990; Qiao and Weisberg 1995, 1998; Wang et al., 2020). Regarding the baroclinic instability mechanism, the equatorial SST front has been suggested to form another important energy source for the TIWs through the conversion of available potential energy (APE), especially north of the equator (Cox 1980; Luther and Johnson 1990; Yu et al., 1995; Masina et al., 1999). A recent analysis of numerical simulation by Wang et al. (2017) also suggested that the energy released by the two instabilities has an almost equal contribution to the generation of TIW EKE. Although much work has been done to understand the general mechanisms of TIWs, the dynamical differences between the two different meridional modes, i.e., the Yanai-mode and the Rossby-mode TIWs, are not fully understood. Wang et al. (2020) examined the energy sources of the two TIW modes and concluded that both the Yanai-mode and the Rossby-mode TIWs are primarily generated by barotropic instability. However, their study only considered the surface layer (0–30 m), without considering the subsurface layer (~30–200 m) in which the two TIW modes still have strong signals. In addition to instability processes, nonlocal energy fluxes have also been found to contribute significantly to the regional EKE budget during the generating and growing processes of TIWs (Luther and Johnson 1990; Masina et al., 1999; Holmes and Thomas 2016). Masina et al. (1999) first noted that there exists significant energy radiation from the north of the equator to the south of the equator by pressure work. Up to now, the role of nonlocal processes such as advection and pressure work in determining the spatial patterns of TIW EKE and coupling of the meridional TIW modes, is still unclear. This makes our first motivation for the present study.

Another motivation concerns the vertical structure of TIWs, which has attracted less attention so far. TIWs are generally considered surface-intensified waves (Lyman et al., 2007). However, observations have shown the existence of subsurface-intensified (peaking at 70–90 m) TIWs in the equatorial Pacific (Liu et al., 2019a) as well as in the Atlantic (Specht et al., 2021). Halpern et al. (1988) discovered that forced by local wind stress, meridional velocity is maximized in the surface (subsurface) layer during the northward (southward) phase of TIWs in the Atlantic. With similar seasonally-varying wind stress (cf., Wang et al., 2017), this phenomenon could also occur in TIWs in the Pacific. All these phenomena imply complex vertical structures of TIWs. A natural question is whether there exists a connection between the surface and subsurface TIWs. And, if so, what is the underlying mechanism for establishing the connection?

To address the above issues, in the following we first briefly introduce a newly developed functional analysis tool, namely, the multiscale window transform (MWT) and the MWT-based localized multiscale energetics analysis and canonical transfer theory (Liang 2016) in section 2, and then the data used for this study (section 3). In Section 4.1, based on the KE spectra in the equatorial Pacific, we decompose the original fields into three scale windows. The three-dimensional structure of the TIW-scale EKE is analyzed in section 4.2. We examine the time and zonal mean TIW-scale KE budget in section 4.3, and then further quantify the spatial coupling of the energetics among different TIW-mode regions and vertical layers in section 4.4. Moreover, the seasonality of the energy pathway is examined in section 4.5. The whole study is summarized in section 5.

2. Methodology

2.1. Multiscale window transform

When studying the multiscale energetics for time-varying and nonstationary processes, many researchers use filters to perform scale decomposition and then take the square of the filtered field as the corresponding local multiscale energy. Take the example which has been used in many previous studies for illustration (e.g., Xu and Liang 2020; Yang et al., 2021b), a velocity field $u(t)$ can be filtered into two parts:

$$u(t) = u^{'}(t) + \overline{u}(t), \tag{1}$$

where $u^{'}(t)$ denotes the eddy part and $\overline{u}(t)$ the background part. A natural question is what is the energy of the two filtered parts? A common practice is simply to take the square of the filtered field (up to some constant factor) as the energy of the corresponding filtered part. This is, unfortunately, incorrect because $[u(t)]^2 = [\overline{u}(t)]^2 + [u^{'}(t)]^2$, i.e., the total energy is not conserved. In fact, multiscale energy is a concept in phase space (e.g., Fourier space); it is related to physical space through Parseval's theorem (Liang 2016). To systematically address this problem, Liang and Anderson (2007) developed the multiscale window transform (MWT). They realized that for a class of specially devised orthogonal filters, just as in the Fourier transform and the inverse Fourier transform, there exists a transform-reconstruction pair. This pair is MWT and its counterpart, Multiscale Window Reconstruction (MWR). MWR functions like a traditional filter, while MWT gives coefficients that are essential to represent the energy of the filtered field. Note that traditional filters do not yield coefficients. MWT can split a function space into a direct sum of several mutually orthogonal subspaces (hereafter referred to as scale window ϖ, window ϖ for brevity), each with an exclusive range of time scales. In this study, we define three scale windows, namely, a low-frequency background flow window (denoted by $\varpi = 0$, with periods longer than 48 days), a TIW window ($\varpi = 1$, with periods between 12 and 48 days), and a high-frequency window ($\varpi = 2$, with periods shorter than 12 days). The reason for the frequency ranges of windows will be explained in section 4.1. For each MWR of a time series $u(t)$, denoted by $u^{\sim\varpi}(t)$, the application of MWT to $u(t)$ will yield a time series of MWT coefficients, denoted by $\widehat{u}_n^{\sim\varpi}$, where $\widehat{(\cdot)}_n^{\sim\varpi}$ denotes MWT on window ϖ at sampling time step n. For two processes on distinct scale windows as shown in Eq. (1), the energy on each window is proportional to the square of the MWT coefficients, i.e., $(\widehat{u}_n^{\sim 0})^2$ and $(\widehat{u}_n^{\sim 1})^2$.

Within the MWT framework, the kinetic energy (KE) K_n^{ϖ} and the available potential energy (APE) A_n^{ϖ} on window ϖ can be expressed as

$$K_n^{\varpi} = \frac{1}{2}\rho_0 \widehat{\boldsymbol{u}}_{h,n}^{\sim\varpi} \cdot \widehat{\boldsymbol{u}}_{h,n}^{\sim\varpi}, \tag{2}$$

and

$$A_n^{\varpi} = \frac{C}{2}\left(\widehat{\rho}_n^{\sim\varpi}\right)^2, \tag{3}$$

where $\boldsymbol{u}_{h,n}$ is the horizontal velocity, $\rho_0 = 1\,025\ \mathrm{kg\ m^{-3}}$ the constant reference density, ρ_n the density perturbation after subtracting a reference density profile $\overline{\rho}(z)$ (time and area mean at each depth) from the original density field, and the factor $C = \frac{g^2}{\rho_0{}^2 N^2}$ ($N = \sqrt{-\frac{g}{\rho_0}\frac{\partial \overline{\rho}}{\partial z}}$; $g = 9.8\ \mathrm{m\ s^{-2}}$) is introduced for convenience. Note that the APE in Eq. (3) is defined under the classical quasi-geostrophic approximation framework (Pedlosky 1979; Oort et al., 1989). For notational brevity, the subscript n will be omitted henceforth.

2.2. *Localized multiscale energetics analysis*

From the primitive equations and Eq. (2), Liang (2016) derived the time evolution equation for K^{ϖ} as follows (for detailed derivation, refer to Liang, 2016):

$$\frac{\partial K^{\varpi}}{\partial t} = \underbrace{\left\{ -\nabla\cdot\left[\frac{\rho_0}{2}\widehat{(\boldsymbol{u}\boldsymbol{u}_h)}^{\sim\varpi}\cdot\widehat{\boldsymbol{u}_h}^{\sim\varpi}\right]\right\}}_{-\nabla\cdot\boldsymbol{Q}_K^{\varpi}} + \underbrace{\left[-\nabla\cdot\left(\widehat{\boldsymbol{u}}^{\sim\varpi}\cdot\widehat{p}^{\sim\varpi}\right)\right]}_{-\nabla\cdot\boldsymbol{Q}_P^{\varpi}} \tag{4}$$

$$+\underbrace{\left(-g\hat{\rho}^{\sim\varpi}\hat{w}^{\sim\varpi}\right)}_{-b^{\varpi}}+\underbrace{\frac{\rho_0}{2}\left[(\boldsymbol{u}\hat{\boldsymbol{u}}_h)^{\sim\varpi}:\nabla\hat{\boldsymbol{u}}_h^{\sim\varpi}-\nabla\cdot(\boldsymbol{u}\hat{\boldsymbol{u}}_h)^{\sim\varpi}\cdot\hat{\boldsymbol{u}}_h^{\sim\varpi}\right]}_{\Gamma_k^{\varpi}}+F_K^{\varpi},$$

where $\boldsymbol{u} = (u, v, w)$ is velocity, p pressure, and the colon : represents the double-dot product of two dyads. This equation indicates that the local tendency of K^{ϖ} on window ϖ is controlled by the multiple energetic processes on the right-hand side of the equation: $-\nabla\cdot\boldsymbol{Q}_K^{\varpi}$ is the convergence of the K^{ϖ} flux, representing the nonlocal transport (i.e., advection) of K^{ϖ}; $-\nabla\cdot\boldsymbol{Q}_P^{\varpi}$ denoting the pressure flux convergence (or pressure work) is another nonlocal energy transport process; $-b^{\varpi}$ is the buoyancy conversion, representing conversion from A^{ϖ} to K^{ϖ} when it is positive; Γ_K^{ϖ} is the transfer of KE to window ϖ from other windows, representing the KE redistribution across different scales.

Similarly, the time evolution equation for the A^{ϖ} can be obtained from the primitive equations and Eq. (3):

$$\frac{\partial A^{\varpi}}{\partial t} = \underbrace{\left\{ -\nabla\cdot\left[\frac{C}{2}\widehat{\rho}^{\sim\varpi}\widehat{(\boldsymbol{u}\rho)}^{\sim\varpi}\right]\right\}}_{-\nabla\cdot\boldsymbol{Q}_A^{\varpi}} + \underbrace{\frac{C}{2}\left[\widehat{(\boldsymbol{u}\rho)}^{\sim\varpi}\cdot\nabla\widehat{\rho}^{\sim\varpi}-\widehat{\rho}^{\sim\varpi}\nabla\cdot\widehat{(\boldsymbol{u}\rho)}^{\sim\varpi}\right]}_{\Gamma_A^{\varpi}}$$

$$-\underbrace{\left(-g\hat{\rho}^{\sim\varpi}\hat{w}^{\sim\varpi}\right)}_{-b^{\varpi}}+F_A^{\varpi}. \tag{5}$$

Similar to Eq. (4), this equation indicates that the local tendency of A^{ϖ} is controlled by the following processes: $-\nabla\cdot\boldsymbol{Q}_A^{\varpi}$ is the convergence of the A^{ϖ} flux, representing the spatial transport of A^{ϖ}; $-b^{\varpi}$ is the buoyancy conversion; Γ_A^{ϖ} is the transfer of APE from other windows to window ϖ. The residual terms F_K^{ϖ} and F_A^{ϖ} include all the external forcings, friction, and unresolved subgrid-scale processes.

The cross-scale transfers (i.e., Γ_K^{ϖ} and Γ_A^{ϖ}) satisfy the following conservation law, as rigorously proved by Liang (2016):

$$\sum_n \sum_{\varpi} \Gamma_n^{\varpi} = 0, \tag{6}$$

which indicates that the cross-scale transfer adds up to 0 after summing over all the sampling time steps n and windows ϖ, suggesting that the cross-scale transfers neither consume nor produce energy; i.e., they only redistribute energy in the phase (frequency) space. This seemingly obvious fact, however, does not hold in other traditional formalisms. Γ_n^{ϖ} thence has been termed "canonical transfer" (Liang 2016).

Note that Γ_K^{ϖ} and Γ_A^{ϖ} in Eqs. (4) and (5) are still in cumulated forms. They need to be further decomposed to obtain the various window-window interactions embedded in the three-scale window framework, which is called "interaction analysis", explained in detail in Liang and Robinson (2005). Take the TIW window ($\varpi = 1$) for example. Liang and Robinson (2005) found that Γ^1 (can be Γ_K^1 or Γ_A^1) can be decomposed as

$$\Gamma^1 = \Gamma^{0\to1} + \Gamma^{2\to1} + \Gamma^{0\oplus2\to1} + \Gamma^{1\to1}. \tag{7}$$

The term $\Gamma^{0\to1}$ represents the energy transfer from window 0 to window 1. In Eqs. (4) and (5), a positive $\Gamma_K^{0\to1}$ ($\Gamma_A^{0\to1}$) means the transfer of KE (APE) from the background flow window to the TIW window, which is proved to correspond precisely to the barotropic (baroclinic) instability defined in the classical Geophysical Fluid Dynamics (Liang and Anderson, 2007). Similarly, the term $\Gamma^{2\to1}$ represents the transfer from window 2 to window 1, and the corresponding KE (APE) transfer is $\Gamma_K^{2\to1}$ ($\Gamma_A^{2\to1}$). A negative $\Gamma_K^{2\to1}$ ($\Gamma_A^{2\to1}$) means a release of K^1 (A^1) to the high-frequency window, indicating a forward energy cascade. The $\Gamma^{0\oplus2\to1}$ term represents the contribution from the window 0-window 2 interaction to window 1. The last term $\Gamma^{1\to1}$ is the transfer within window 1 itself. The last two terms are usually negligible. Based on Eqs. (4) and (5), we can quantitatively analyze the production and redistribution of the TIW energy in the different TIW-mode regions. The methods above have been applied to many realistic problems in the ocean (e.g., Yang et al., 2021a,b; Zhao et al., 2022) and the atmosphere (e.g., Xu and Liang 2020; Zhang and Liang 2021) so far.

3. Data

One of the difficulties in performing energetics analysis from in situ observations, such as the Tropical Atmosphere-Ocean (TAO) mooring array, is that the observational records are sparsely distributed and have substantial missing data, especially at the surface layers above 35 m (Wang et al., 2020), where the surface-trapped mode of the TIWs occurs. In addition, some variables such as vertical velocity and dynamic pressure, which are essential in calculating the full energy budget of the TIWs, cannot be faithfully estimated from the observed ones. For these reasons, outputs from the Hybrid Coordinate Ocean Model with Navy Coupled Ocean Data Assimilation (HYCOM + NCODA, HYCOM henceforth) daily global reanalysis from 2000 to 2015 are used for this study. They are interpolated to the GLBv0.08 grid with a horizontal resolution of $(1/12.5)^{\circ}$ between 40°S – 40°N, and 40 levels in the vertical (Cummings and Smedstad 2013). Several previous studies have used this dataset in studying the TIW dynamics, including Martinez et al. (2018) and Liu et al. (2019a), among others. Since the main part of the TIW EKE is concentrated in the near-surface layer (e.g., Wang et al., 2017, 2019), we use 23 levels of the outputs between 0 and 200 m.

To assess the performance of HYCOM reanalysis, we use daily global surface current data from the Archiving, Validation, and Interpretation of Satellite Oceanographic Data (AVISO), merged from multiple satellite altimeters (Traon et al., 1998), available since 1993 on a $1/4^{\circ} \times 1/4^{\circ}$ grid. We will refer to this dataset as AVISO hereafter. In addition to the above, the hourly velocity data at the equator and 140 °W from the TAO array also will be used (McPhaden 1995).

4. Results

4.1. *Detection of TIW signals and scale decomposition*

Fig. 1a shows the KE power spectra at the surface averaged over the central and eastern equatorial Pacific (180° – 90°W, 8°S – 8°N). The KE spectra based on HYCOM exhibit substantial signals of multiscale processes in the central and eastern equatorial Pacific. For periods shorter than 6 months, the spectra are dominated by a signal of 33 days, corresponding to the Rossby-mode TIWs, and a secondary peak around 17.5 days, corresponding to the Yanai-mode TIWs (Lyman et al., 2007; Wang et al., 2020). In general, the spectra based on HYCOM agree well with those based on AVISO, which demonstrates that HYCOM well captures the observed TIW EKE in the central and eastern equatorial Pacific. Note that the synoptic-scale signals (<10 days) are not well captured by AVISO due to their coarse resolution; they are, though, captured in HYCOM. In addition, around the 17.5 days, KE is significantly smaller in the spectra of AVISO than in HYCOM, which may be related to the fact that the geostrophic balance does not hold within the equatorial band so that the satellite-based geostrophic surface currents cannot well capture the Yanai-mode TIWs near the equator (also found in, e.g., Tuchen et al., 2018).

To assess the performance of HYCOM at the equator, we compare the spectra of KE at (0°, 140°W) and the depth of 10 m based on HYCOM and TAO (Fig. 1b). The spectra are estimated during an intensive observation period spanning 5 May 2002 through 18 January 2006. Although the KE

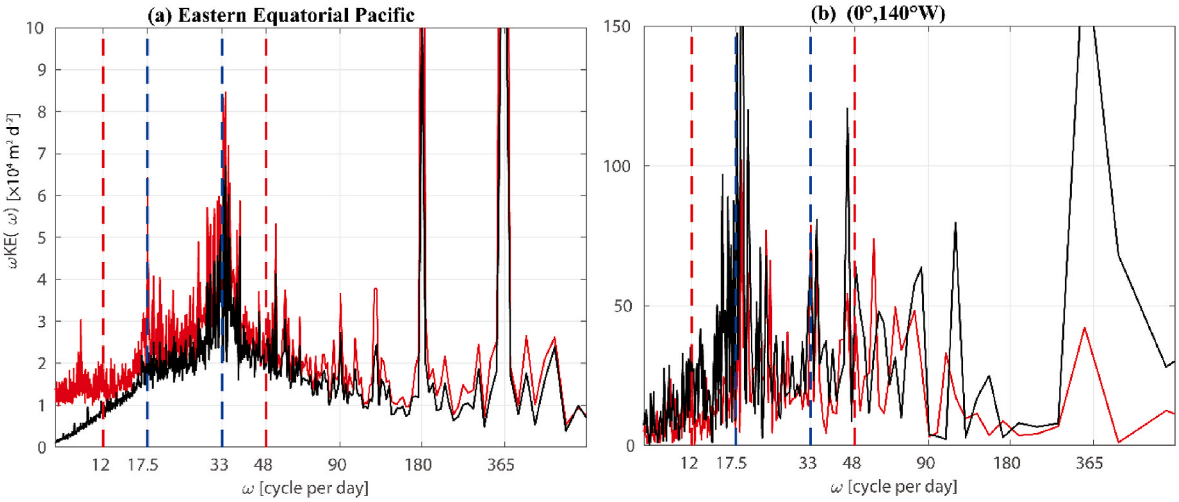

Fig. 1. The frequency spectra (lines) of (a) the surface KE averaged over the eastern equatorial Pacific based on AVISO (black line) and HYCOM (red line) and (b) the KE at $(0^\circ, 140^\circ\mathrm{W})$ and the depth of 10 m based on TAO (black line) and HYCOM (red line). The spectra are plotted in variance-preserving form (i.e., spectrum KE (ω) multiplied by frequency ω). The dashed lines denote the periods of 12, 17.5, 33, and 48 days from left to right respectively. The range of the ordinate is limited to $0-10\ \times 10^4\ \mathrm{m^2 d^{-3}}$ in (a) and $0-150\ \times 10^4\ \mathrm{m^2 d^{-3}}$ in (b) to highlight the high-frequency spectra.

based on HYCOM is generally smaller than that based on TAO, both spectra are dominated by the signal around 17.5 days, corresponding to the Yanai-mode TIWs. This demonstrates that HYCOM is able to reasonably simulate the observed TIW EKE at the equator.

Based on the above spectrum analysis, we set the time scale window for TIWs as 12–48 days, which includes both the Yanai-mode and the Rossby-mode. We apply MWT to decompose the original fields into three windows, which are referred to as the low-frequency background flow window ($\varpi = 0$, with periods longer than 48 days), the TIW window ($\varpi = 1$, with periods between 12 and 48 days), and the high-frequency window ($\varpi = 2$, with periods shorter than 12 days).

4.2. *Three-dimensional structure of the TIW-scale EKE*

Fig. 2 shows the long-term mean horizontal and vertical distributions of the TIW-scale EKE (K^1) from the HYCOM reanalysis data, which reveals a meridional double-peak structure. At both the depths of 0 m and 100 m, K^1 is concentrated along two zonally elongated zones which are $170^\circ-95^\circ\mathrm{W}, 2^\circ\mathrm{S}-1^\circ\mathrm{N}$ and $170^\circ-110^\circ\mathrm{W}, 1^\circ-7^\circ\mathrm{N}$. Fig. 3 displays the power spectra of meridional velocity in the two zones. It can be seen that the meridional velocity peaks around 17.5 days in the region of $170^\circ-95^\circ\mathrm{W}, 2^\circ\mathrm{S}-1^\circ\mathrm{N}$ (Fig. 3a) and 33 days in the region of $170^\circ-110^\circ\mathrm{W}, 1^\circ-7^\circ\mathrm{N}$ (Fig. 3b), consistent with previous observational studies (e.g., Lyman et al., 2007; Wang et al., 2020). This provides further evidence of the high reliability of the HYCOM simulation. In the following, we refer to the regions of $170^\circ-95^\circ\mathrm{W}, 2^\circ\mathrm{S}-1^\circ\mathrm{N}$ and $170^\circ-110^\circ\mathrm{W}, 1^\circ-7^\circ\mathrm{N}$ as the Yanai-mode and Rossby-mode regions, respectively. Fig. 2c shows the vertical structure of K^1 averaged along the $180^\circ-90^\circ\mathrm{W}$ band. The surface-intensified K^1 signal extends to about 180 m depth in the Yanai-mode region and about 120 m depth in the Rossby-mode region. It is worth mentioning that there exists a slight northward vertical tilting with depth in the K^1 field in both mode regions. In the Yanai-mode region, K^1 is strongest at the surface of the equator and the depth of 100 m near 1°N; in the Rossby-mode region, K^1 maximizes at the surface of 3°N and the depth of 100 m near 4°N. In other words, the maximum centers of K^1 move northward about 1° from surface to subsurface in both regions. These results suggest that the TIW variability has complex vertical structures.

To see the vertical coherence of the TIW EKE signals, we plot the

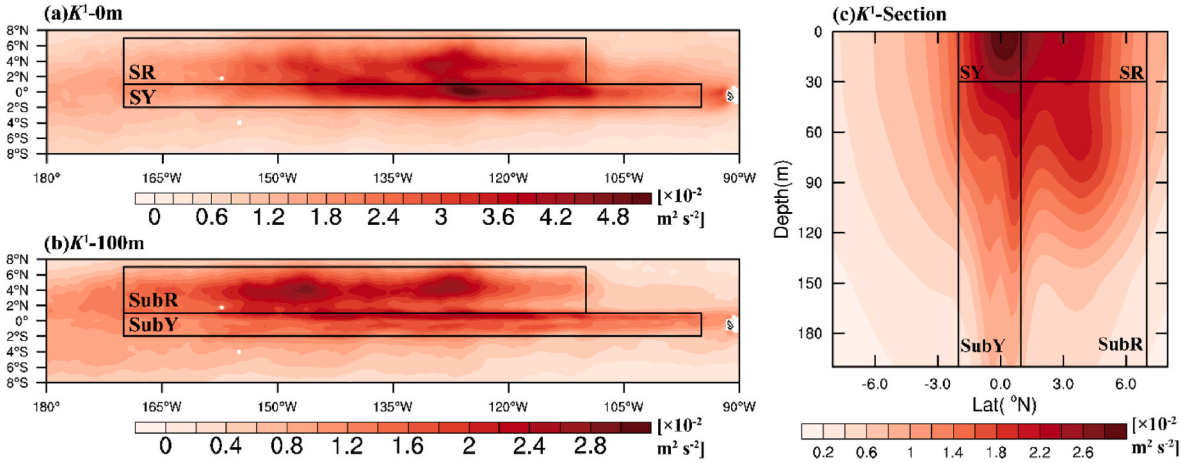

Fig. 2. (a–b) Time-mean maps of the TIW EKE (K^1, shadings) at (a) 0 m and (b) 100 m. The two black boxes labeled SY and SR (SubY and SubR) in (a) [(b)] refer to the subdomains in the text: the Yanai-mode region ($170^\circ-95^\circ\mathrm{W}, 2^\circ\mathrm{S}-1^\circ\mathrm{N}$) and the Rossby-mode region ($170^\circ-110^\circ\mathrm{W}, 1^\circ-7^\circ\mathrm{N}$) at the surface (subsurface) layer respectively. (c) Time-mean depth-latitude section of K^1 (shadings) averaged over the $180^\circ-90^\circ\mathrm{W}$ band. The SY and SR (SubY and SubR) black boxes in (c) are defined between 0 and 30 m (30–200 m).

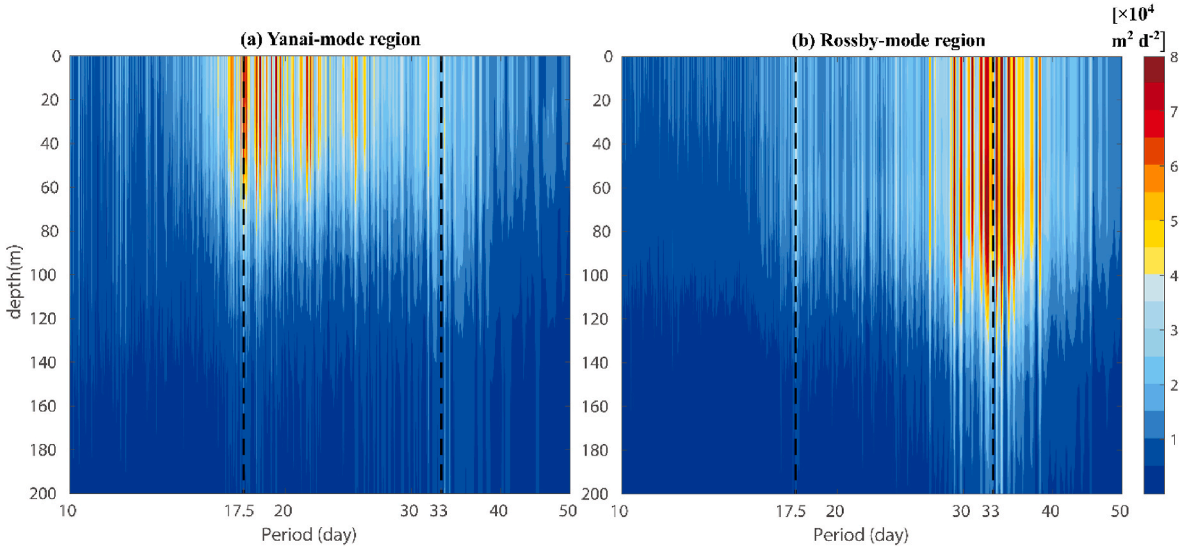

Fig. 3. Vertical distributions of the meridional velocity energy spectra (shadings) in (a) the Yanai-mode region and (b) the Rossby-mode region. The black dashed lines denote the periods of 17.5 and 33 days, respectively.

vertical distributions of the correlation coefficients between the EKE time series at depth and that at the surface (Fig. 4). It can be seen that the correlation coefficient in the Rossby-mode region exceeds 0.93 at all depths (blue line in Fig. 4), suggesting a strong vertical coherence of the EKE variability in this region. In contrast, the vertical coherence of the EKE times series is weaker in the Yanai-mode region; the correlation drops strongly below 60 m (red line in Fig. 4). One possible reason for this decorrelation could be the presence and eastward propagation of Yanai waves below the surface layer (Ascani et al., 2015; Tuchen et al., 2018; Körner et al., 2022). The black line in Fig. 4 shows the correlation between the EKE time series at each depth between the two mode regions. It shows that there is a strong connection between the EKE variability in the two mode regions, suggesting a horizontal coherence of the EKE variability between the two regions.

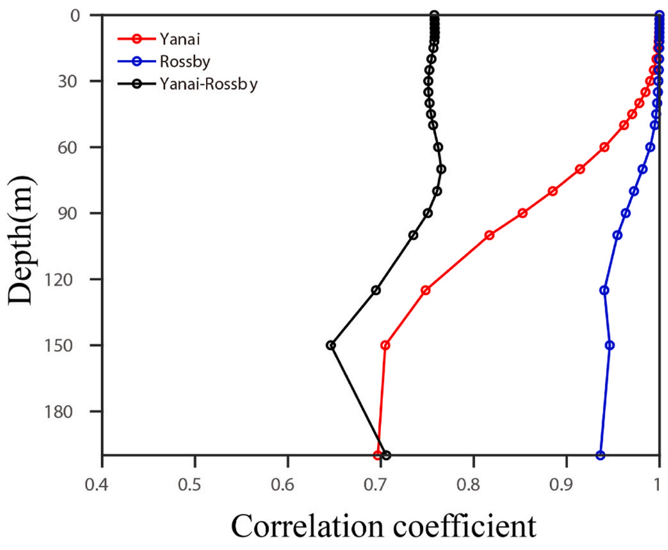

Fig. 4. EKE coherence levels as a function of depth. Red (blue) line: correlation between the K^1 time series at depth with that at the surface for the Yanai (Rossby) mode region. Black line: correlation between the K^1 time series in the Yanai-mode region with that in the Rossby-mode region. The K^1 time series are averaged over the Yanai- and Rossby-mode regions as defined in Fig. 2.

4.3. Time and zonal mean TIW-scale KE budget analysis

In this section, we present the long-term mean (2000–2015) and zonal mean TIW-scale kinetic energy budget based on the HYCOM reanalysis data, in order to understand how TIWs are generated and coupled vertically and horizontally. For easy reference, the energy terms used for the following analysis and their physical meaning are summarized in Table 1.

Fig. 5 shows the depth-latitude distributions of the TIW-scale energy budget terms that are averaged over the zonal band of $180^\circ - 90^\circ$W. We first examine the role of barotropic instability in governing the long-term mean TIW variability. Recall that a positive barotropic canonical transfer $\Gamma_K^{0\to1}$ indicates a KE transfer from the background flow to TIWs via barotropic instability, whereas for a negative $\Gamma_K^{0\to1}$ indicates a KE transfer from TIWs to the background flow. From Fig. 5a, it can be seen that $\Gamma_K^{0\to1}$ is mostly positive in the Yanai-mode region between 0 and 200 m and the Rossby-mode region between 0 and 90 m. The positive $\Gamma_K^{0\to1}$ is mainly located in the meridional shear region between the NECC and SEC and between the EUC and SEC. This indicates that the equatorial currents are barotropically unstable, resulting in strong KE transfer to TIWs from the meridionally sheared currents, consistent with previous studies (Philander 1976, 1978; Cox 1980; Luther and Johnson 1990; Qiao and Weisberg 1995, 1998; Wang et al., 2020). Besides the dominant positive transfer, there is a negative pool of $\Gamma_K^{0\to1}$ occupying south of the equator at the surface layer (0–40 m), indicating that the TIWs transfer their kinetic energy back to the background currents in this region.

In the following, we examine another generation mechanism, i.e., baroclinic instability, to see its role in governing the long-term mean TIW variability. The APE stored in the background flow can be released to the TIW variability and subsequently converted to K^1 through the baroclinic instability energy pathway (i.e., $A^0 \to A^1 \to K^1$), in which the positive APE transfer matrix $\Gamma_A^{0\to1}$ represents an APE transfer from the background flow to TIWs ($A^0 \to A^1$) and the positive buoyancy conversion $-b^1$ represents the conversion from the TIW APE to the TIW EKE ($A^1 \to K^1$). As revealed in Fig. 5b and c, both $\Gamma_A^{0\to1}$ and $-b^1$ feature overwhelmingly positive values near the equator as well as the north of the equator, indicating that the APE of the background flow is released to generate TIWs via baroclinic instability, consistent with previous studies (Cox 1980; Luther and Johnson 1990; Yu et al., 1995; Masina et al., 1999; Wang et al., 2017). It is worth noting that, within the upper

Table 1

Physical meaning of the energy terms used for analysis.

Symbol	Meaning
K^1	TIW-scale Eddy Kinetic Energy (TIW EKE)
A^1	TIW-scale Available Potential Energy (TIW APE)
$\Gamma_K^{0\to1}$	Canonical transfer of KE from the background flow to TIWs
$\Gamma_K^{2\to1}$	Canonical transfer of KE from the high-frequency fluctuations to TIWs
$\Gamma_A^{0\to1}$	Canonical transfer of APE from the background flow to TIWs
$-b^1$	Buoyancy conversion from TIW APE to TIW EKE
$-\nabla\cdot\boldsymbol{Q}_K^1$	Advective TIW EKE spatial transport
$-\nabla_h\cdot\boldsymbol{Q}_P^1$	Horizontal pressure work
$-\nabla_z\cdot\boldsymbol{Q}_P^1$	Vertical pressure work
F_K^1	Residue terms of the TIW EKE budget equation including forcing and dissipation processes

30 m, there is a mismatch between the two terms: the baroclinic transfer $\Gamma_A^{0\to1}$ is strong, while the buoyancy conversion $-b^1$ is only of moderate strength. This seems to imply that a large part of A^1 transferred from the background APE is not efficiently converted into K^1 in the surface layer. However, the large amplitude of $\Gamma_A^{0\to1}$ should be interpreted with caution since we adopt the quasi-geostrophic definition of APE, which might not be accurate enough at the ocean surface due to large density perturbation and weak stratification in this layer. Anyway, we can use the second phase of the baroclinic instability energy pathway, i.e., $A^1\to K^1$ (or $-b^1$), to estimate the strength of baroclinic instability. The buoyancy conversion $-b^1$ has a substantial amplitude over $1^\circ-5^\circ$N between 10 m and 90 m, and a relatively weak amplitude at the surface and near the equator. The positive $-b^1$ is mainly located on the equatorial front, where the meridional density share is large. This indicates that baroclinic instability is an important energy source for the generation of TIWs in the Rossby-mode region, while its contribution is moderate for the growth of the TIWs in the Yanai-mode region. It is worth mentioning that the barotropic and baroclinic energy productions of TIWs have been shown to be only maximized near the surface in the Equatorial Atlantic (Schuckmann et al., 2008), not at subsurface layers as found in the Pacific Ocean. This difference is likely to be associated with the different vertical extent and strength of the EUC in the two ocean sectors. The EUC extends much deeper with larger zonal velocity in the Pacific than that in the Atlantic (Compare our Figs. 5a to 10a in Schuckmann et al., 2008), which produces stronger horizontal shear in the subsurface layer of the Equatorial Pacific, and hence larger energy production rate through barotropic instability there. Similarly, the deep-reaching baroclinic energy production near 3°N is related to the large meridional gradient of density there (Fig. 5c).

The three-scale energetics framework also enables us to examine the interaction between TIWs and the high-frequency fluctuations. As introduced in section 2, when the transfer matrix $\Gamma_K^{2\to1}$ is negative, it represents that TIWs release KE to the high-frequency fluctuations via the forward KE cascade. The negative values of $\Gamma_K^{2\to1}$ indicate the high-frequency fluctuations mainly act to extract energy from the K^1 reservoir (Fig. 5d). Note that this happens only close to the surface and that the magnitude of $\Gamma_K^{2\to1}$ is about one order smaller than that of $\Gamma_K^{0\to1}$, suggesting that only a small portion of K^1 close to the surface is dissipated through the forward energy cascade to the high-frequency fluctuations.

The above results reveal the relative contributions of barotropic and baroclinic instabilities to the TIW variability in the surface and subsurface layers of the Yanai-mode and Rossby-mode regions. In the subsurface layer (30–200 m) of the Yanai-mode (Rossby-mode) region, we find that barotropic (baroclinic) instability dominates. In the surface layer (above 30 m) of the Rossby-mode region, both barotropic and baroclinic instabilities are important energy sources for the TIW variability. It is interesting to note that in the surface layer of the Yanai-mode region, especially south of the equator, there exists a pool of negative canonical barotropic transfer, suggesting that TIWs lose their K^1 here to the background flow. Meanwhile, the energy released by baroclinic instability is quite low. This suggests that instability processes alone cannot explain the TIW dynamics in the surface layer of the Yanai-mode region, in which substantial amplitudes of EKE is observed (Fig. 2c).

We therefore look at the nonlocal processes which are presented as $-\nabla\cdot\boldsymbol{Q}_P^1$ and $-\nabla\cdot\boldsymbol{Q}_K^1$ in the K^1 budget equation. $-\nabla\cdot\boldsymbol{Q}_P^1$ is the dominant nonlocal term which is further decomposed into its horizontal ($-\nabla_h\cdot\boldsymbol{Q}_P^1$) and vertical ($-\nabla_z\cdot\boldsymbol{Q}_P^1$) components since the vertical component has been recently reported to be important to couple the eddy energetics in the vertical direction (e.g., Yang et al., 2021a). The $-\nabla_z\cdot\boldsymbol{Q}_P^1$ maximizes in the Rossby-mode region and exhibits a distinct dipolar structure in the vertical plane (Fig. 5e), positive in the surface layer (above ~30 m) and negative in the subsurface layer (below 30 m). To see how this process redistributes energy in the vertical direction, we additionally draw in Fig. 5e the vertical component of pressure flux $\boldsymbol{Q}_{P,z}^1$ as arrows. Clearly, $\boldsymbol{Q}_{P,z}^1$ is dominantly upward over $1^\circ-4^\circ$N, which leads to the convergence near the surface and the divergence between 30 m and 125 m, corresponding to the positive and the negative pattern of $-\nabla_z\cdot\boldsymbol{Q}_P^1$ as shown in Fig. 5e. Further north ($5^\circ-7^\circ$N), $\boldsymbol{Q}_{P,z}^1$ is weakly downward from the surface to the depth of 100 m. Regarding the horizontal pressure work, there is an array of alternating positive and negative $-\nabla_h\cdot\boldsymbol{Q}_P^1$ patches in the horizontal direction (Fig. 5f). Particularly, $-\nabla_h\cdot\boldsymbol{Q}_P^1$ maximizes in the upper 60-m depth, with positive values in the Yanai-mode region and negative values in the Rossby-mode region, indicating that $-\nabla_h\cdot\boldsymbol{Q}_P^1$ serves as a source (sink) of EKE in the Yanai-mode (Rossby-mode) region in the upper 60 m. From the horizontal vectors of $\boldsymbol{Q}_{P,y}^1$, one can see that there exists a strong southward energy flux from the Rossby-mode region to the Yanai-mode region in the surface layer. In addition, $\boldsymbol{Q}_{P,y}^1$ is weakly northward from the south of 1°S to the equator in the upper 30-m depth and from 5°N to the north of 6°N between 30 m and 90 m. The advection term $-\nabla\cdot\boldsymbol{Q}_K^1$ also acts to redistribute K^1 but has a weaker amplitude than the pressure work (Fig. 5g). $-\nabla\cdot\boldsymbol{Q}_K^1$ is positive south of 1°S and north of 4°N, and negative at the equator and over $1^\circ-3^\circ$N, indicating that K^1 is mainly advected from the core region of TIWs to its surrounding regions.

The residue term F_K^1 exhibits large negative values (Fig. 5h). Since F_K^1 is treated as a residue term that includes all forcing and dissipation processes, it is not possible to distinguish which process is responsible for the K^1 sink at this stage. We conjecture that the surface intensified negative F_K^1 could be a result of EKE damping by wind stress since a number of previous studies have suggested that surface wind stress tends to damp the activity of TIWs (e.g., Pezzi et al., 2004; Seo et al., 2007; Zhang 2014). In the interior ocean, F_K^1 is also a major sink of the TIW EKE, possibly through internal turbulent dissipation. An exception is the subsurface layer of the Rossby-mode region, where the dominant EKE sink is due to outward energy flux by horizontal as well as vertical pressure work.

The TIW-scale EKE budget analysis presented above highlights the nonlocal pressure work process in determining the spatial pattern of the

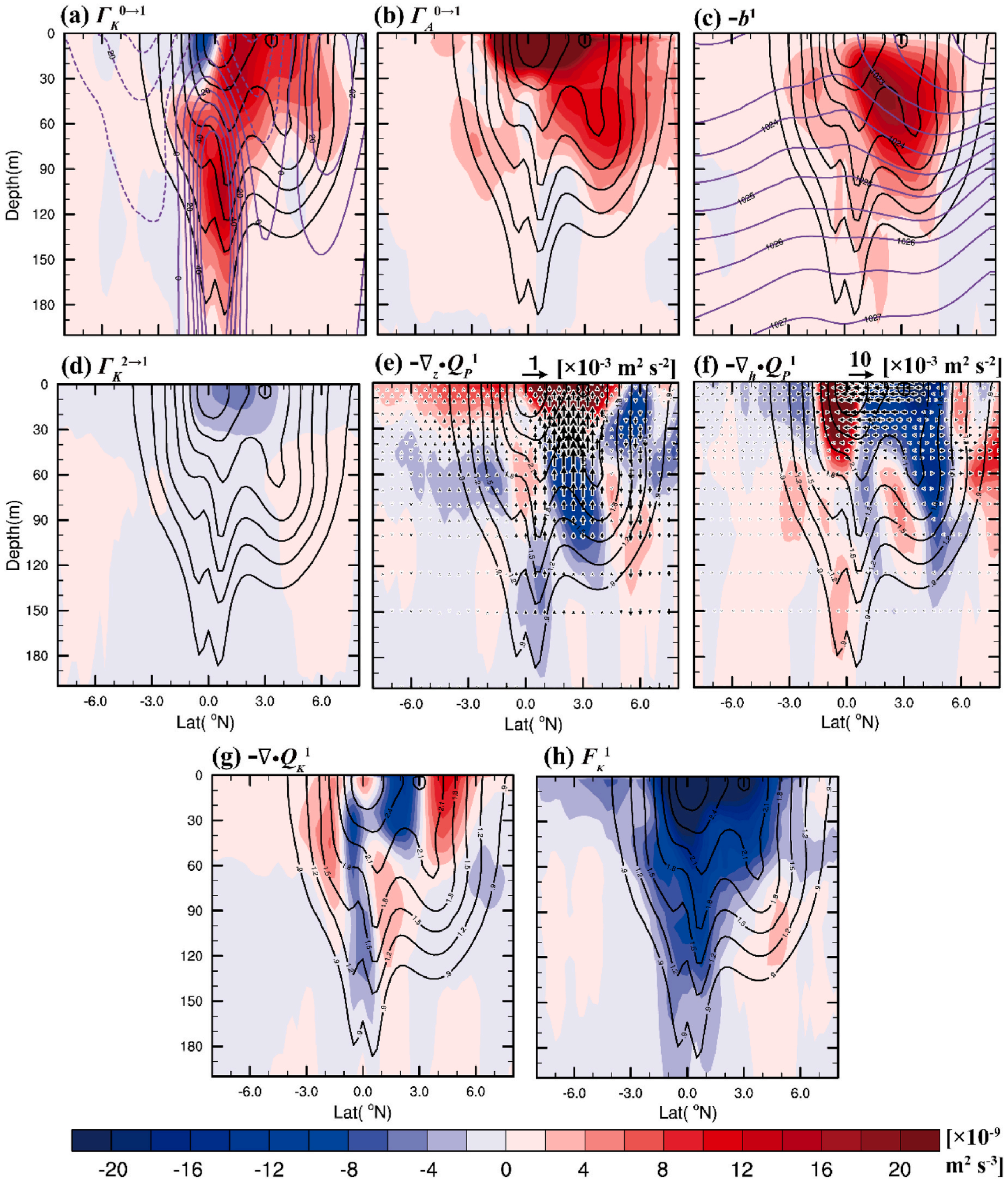

Fig. 5. Time-mean depth-latitude sections of the energy terms (shadings). Refer to Table 1 for the meaning of each energy term. Superimposed vectors in (e) and (f) are the meridional component of pressure flux ($Q^1_{P,y}$) and the vertical component of pressure flux ($Q^1_{P,z}$), respectively. Zonal velocity [purple contours, solid (dashed) contours indicating westward (eastward) velocity, 10^{-2} m s^{-1}] and density (purple contours, kg m^{-3}) are superimposed in (a) and (c), respectively. K^1 (black contours) is superimposed on all panels.

EKE in the equatorial Pacific. The collocation of negative $-\nabla_z \cdot Q_P^1$ and positive $-b^1$ in the subsurface layer over $1^\circ - 4^\circ$N indicates that the EKE is generated via baroclinic instability in the subsurface layer of the Rossby-mode region and then is transported upward to the surface layer by pressure work. The accumulated EKE in the surface layer of the Rossby-mode region due to combined contributions from mixed barotropic-baroclinic instabilities and upward energy flux is further transported toward the surface layer of the Yanai-mode region, where instability processes are relatively weak. This energy pathway, which has never been documented before, is essential to bridge the energetics of TIWs horizontally as well as vertically. This coupling mechanism also helps to explain why the Rossby-mode TIWs have a higher vertical coherence between the surface and subsurface layers than the Yanai-mode TIWs (Fig. 4).

4.4. *Quantification of the spatial energetic coupling among different TIW-mode regions and vertical layers*

According to the vertical structure of $-\nabla_z \cdot Q_P^1$, we divide the water column into two vertical layers, namely, the surface layer (0–30 m) and the subsurface layer (30–200 m), and present a quantitative description of the coupling of the TIW variability in the vertical and meridional directions. For convenience, we introduce four subdomains: the surface layer of the Yanai-mode region (SY), the subsurface layer of the Yanai-mode region (SubY), the surface layer of the Rossby-mode region (SR), and the subsurface layer of the Rossby-mode region (SubR). Refer to Fig. 2 for the extent of the subdomains. Fig. 6 shows the schematic diagram of the energy pathways in terms of volume-integrated TIW energy budgets for the four subdomains. It is found that instability processes play the leading role in generating EKE in the subsurface layer. However, the dominant instability differs in the two TIW-mode regions. The barotropic instability pathway (i.e., $K^0 \rightarrow K^1$) is the dominant EKE generation mechanism in SubY, accounting for 61% of the total K^1 sources, while this pathway is the secondary in SubR, accounting for 38% of the total K^1 sources. In contrast, the baroclinic instability pathway (i.e., $A^0 \rightarrow A^1 \rightarrow K^1$) dominates the EKE generation in SubR, accounting for 62% of the total K^1 sources, while it is the secondary in SubY, accounting for 23% of the total K^1 sources.

Different from the subsurface layer, the nonlocal mechanism fulfilled by pressure work is prominent in the surface layer. Strong southward (upward) energy flux facilitated by pressure work is observed in SY (SR), accounting for 49% (40%) of the total K^1 sources. Besides, northward (14%) and upward (18%) energy fluxes are energy sources in SY as well. In contrast, instability mechanisms play a secondary role in this layer, especially in SY, where the two instabilities contribute about 17% of the total K^1 sources. In SR, instabilities are more important. Here, upward pressure flux, barotropic energy transfer, and baroclinic energy transfer are the three dominant sources of K^1 in this subdomain, respectively accounting for 40%, 36%, and 22% of the total K^1 sources.

With regard to the EKE sinks, turbulent viscous stress processes (F_K^1) dominate the EKE sinks in SY, SubY, and SR, accounting for 93%, 72%, and 58% of the total K^1 sinks, respectively. Different from these three subdomains, outward (southward, northward, and upward) pressure flux is the dominant sink of K^1 in SubR, accounting for 70% of the total K^1 sinks. In SR, southward and northward pressure work plays a secondary role in damping K^1, accounting for 34% of the total K^1 sinks. The northward pressure flux in SR and SubR may reflect the poleward radiation of Rossby waves (Flament et al., 1996; Flament et al., 1996). In SubY, upward pressure work plays a secondary role in damping K^1, accounting for 11% of the total K^1 sinks. From a perspective of volume integral of the whole central and eastern equatorial Pacific (0–200 m, $180^\circ - 90^\circ$W; 8°S $-$ 8°N), F_K^1 is the dominant EKE dissipation mechanism, while $\Gamma_K^{2\rightarrow 1}$, $-\nabla \cdot \boldsymbol{Q}_P^1$, and $-\nabla \cdot \boldsymbol{Q}_K^1$ make a minor contribution, accounting for 85%, 6%, 5%, and 4% of the total K^1 sinks, respectively. This suggests that only a small amount of TIW-scale EKE is transported out of the considered domain.

It should also be noted that from the perspective of volume integral of the whole central and eastern equatorial Pacific, baroclinic and barotropic instabilities are indeed the two dominant EKE generation mechanisms, accounting for 51% and 49% of the total K^1 sources, respectively. This result is generally in agreement with previous studies (e.g., Yu et al., 1995; Masina et al., 1999; Wang et al., 2020). However, we stress in this study that the dominant energy pathway could be quite different when different TIW-mode regions and different vertical layers are considered. We further find that the region-dependent TIW energetics in the equatorial Pacific are closely connected through nonlocal energy transports mainly facilitated by pressure work in both horizontal as well as vertical directions. In particular, we find that the large EKE level in SY is not instability driven as suggested in previous studies (e.g., Cox 1980; Luther and Johnson 1990; Qiao and Weisberg 1998; Wang et al., 2020). The EKE budget in this subdomain is significantly nonlocal through horizontal energy flux from SR. Such a nonlocal energy pathway has not been identified in previous studies.

4.5. *Seasonality of the energy pathway*

In the above subsection, we have provided a detailed description of the different K^1 sources (sinks) in the different subdomains from a long-term mean point of view. In this section, we further examine the seasonality of K^1 and its relevant energetics terms, thanks to the temporal localization feature of MWT. Fig. 7 depicts the annual cycles of the dominant TIW energetics terms (colored lines) together with K^1 (black lines) in the four subdomains. It can be seen that K^1 exhibits analogous seasonal variation in the four subdomains, which minimizes in April-May, increases dramatically in June-August, maximizes in September, remains high in October-January, and decreases in February-March, in agreement with previous studies (e.g., Legeckis 1977; Wyrtki 1978). Consistent with the time-mean results, the dominant energy source term in SubY is $\Gamma_K^{0\rightarrow 1}$ which exhibits an annual cycle in phase with K^1 (Fig. 7c), suggesting that the seasonal K^1 is modulated by barotropic instability in this subdomain. In SubR, both $\Gamma_K^{0\rightarrow 1}$ and $-b^1$ reveal a clear seasonal cycle that resembles that of K^1 (Fig. 7d), indicating that the

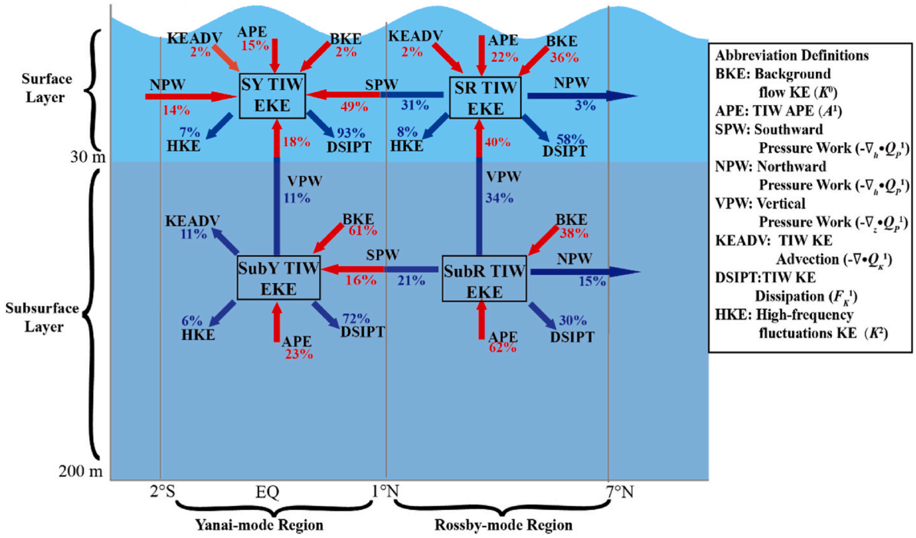

Fig. 6. Schematic of the TIW energetics in the equatorial Pacific Ocean. Percentages mean the contributions to the TIW EKE from respective sources (in red font; represented by red arrows) and sinks (in blue font; represented by blue arrows). HKE and KEADV are omitted in the SubR subdomain since their contribution percentages are below 1%.

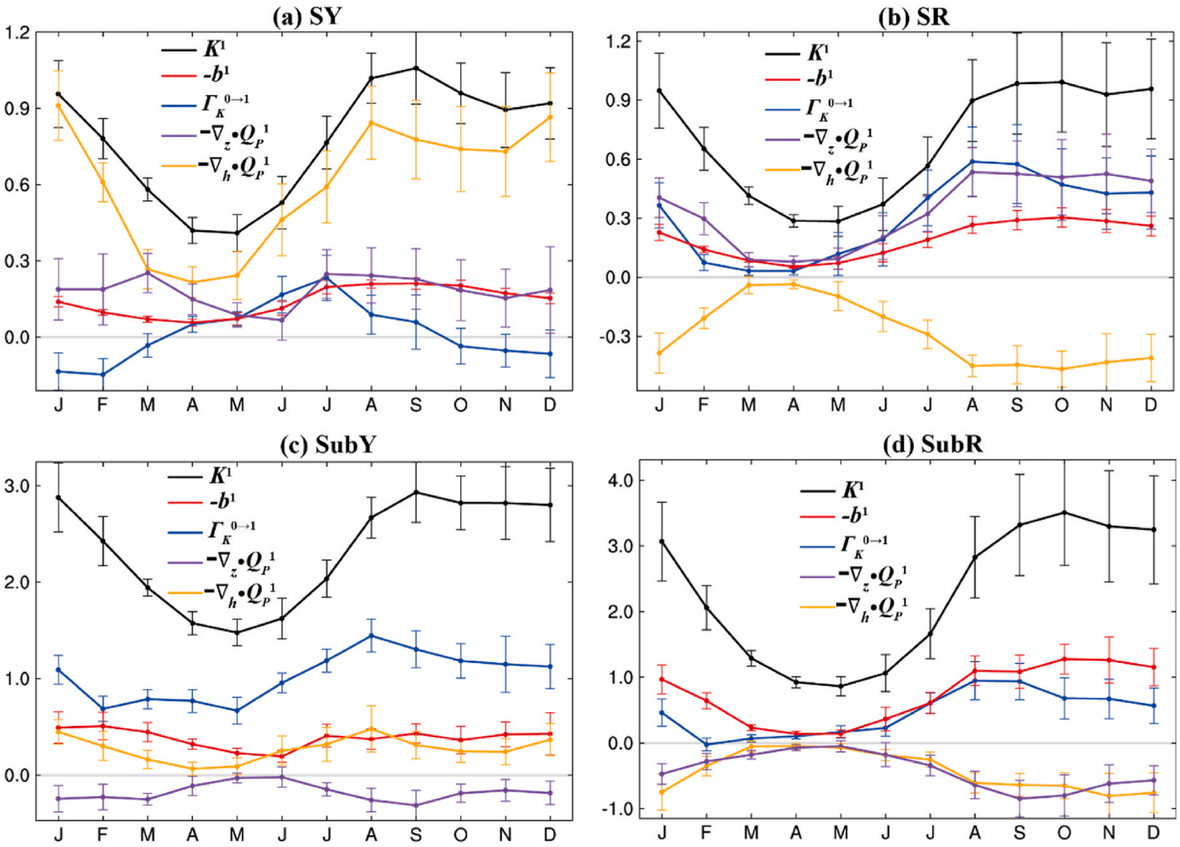

Fig. 7. Climatological annual cycles of K^1 (black lines; m^{3}s^{-2}) and the energy terms (color lines; $\times$ 10^{-6} m^{3}s^{-3}) horizontally averaged over (a) the SY, (b) SR, (c) SubY, (d) SubR subdomains. Refer to Table 1 for the meaning of each energy term. The terms are all vertically integrated from surface to 30 m for (a–b) and from 30 m to 200 m for (c–d). The error bars indicate the 90% confidence band.

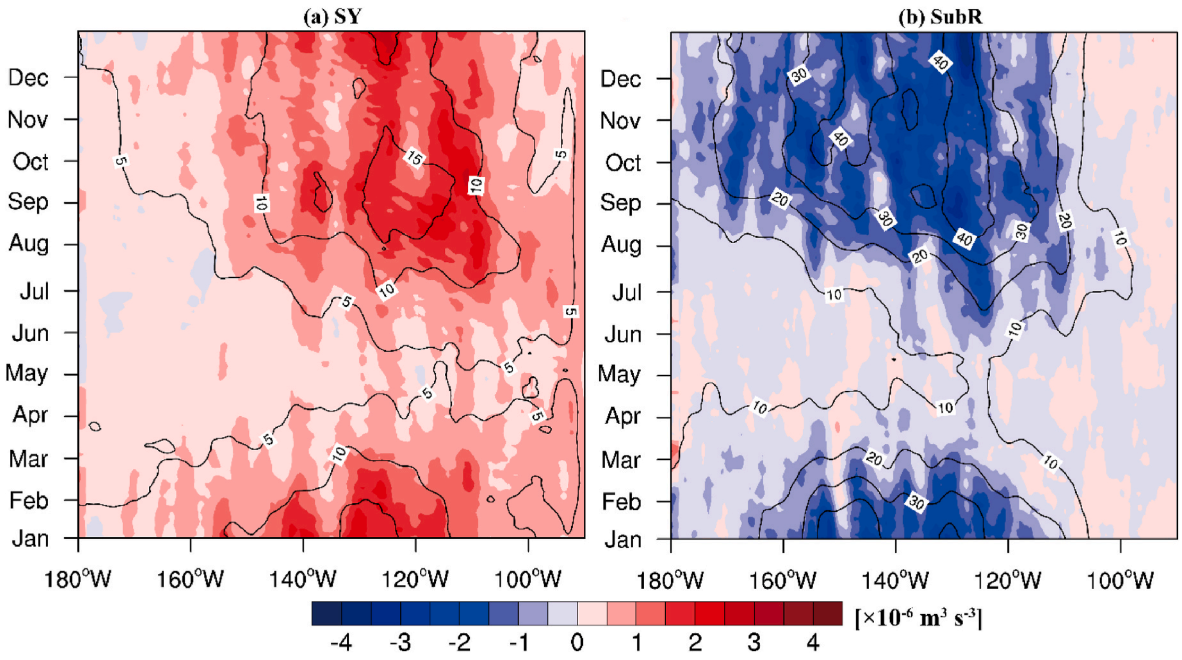

Fig. 8. Seasonal depth-integrated pressure work ($-\nabla\cdot Q_P^1$, shadings) and the TIW EKE (K^1, contours; 10^{-1}m^{3}s^{-2}) for (a) the surface layer averaged between 2°S – 1°N and (b) the subsurface layer averaged between 1° – 7°N. The data have been spatially smoothed by a moving average filter with a horizontal window of 11 by 11 grid points (2.75° × 2.75°).

seasonal K^1 is modulated by mixed barotropic and baroclinic instabilities in this subdomain. Note that $-b^1$ is significantly larger in magnitude than $\Gamma_K^{0\to1}$ during October and December-March (Fig. 7d), suggesting that baroclinic instability dominates K^1 production during this period. This explains the dominance of the baroclinic pathway revealed previously in the time-mean sense (Fig. 6). These results are consistent with Wang et al. (2017) whose work indicates that, from June to December, the development of southerly winds deepens the thermocline trough in the equatorial Pacific, which allows the equatorial currents to strengthen and become more barotropically-baroclinically unstable.

In contrast to the subsurface layer, the seasonal cycle of the K^1 in SY is primarily modulated by $-\nabla_h\cdot\boldsymbol{Q}_P^1$ (Fig. 7a), while that in SR is controlled by the seasonally varying $-\nabla_z\cdot\boldsymbol{Q}_P^1$, $\Gamma_K^{0\to1}$, and $-b^1$ (Fig. 7b). The horizontally inwardly advected energy (positive $-\nabla_h\cdot\boldsymbol{Q}_P^1$) in SY is associated with strong outwardly advected energy (negative $-\nabla_h\cdot\boldsymbol{Q}_P^1$) in SR (see the out-of-phase relation between $-\nabla_h\cdot\boldsymbol{Q}_P^1$ and K^1 in Fig. 7b). Similarly, the seasonal variation of the vertically inwardly advected energy (positive $-\nabla_z\cdot\boldsymbol{Q}_P^1$) in SR is anti-correlated with that of the outwardly advected energy (negative $-\nabla_z\cdot\boldsymbol{Q}_P^1$) in SubR. In addition, a negative correlation is found between the seasonal time series of $-\nabla_h\cdot\boldsymbol{Q}_P^1$ and K^1 in SubR, indicating that $-\nabla_h\cdot\boldsymbol{Q}_P^1$ is also a major sink of K^1 in SubR and partly contributes to the K^1 seasonality in SubY. Fig. 8 further shows the Hovmöller diagram of the evolution of $-\nabla\cdot\boldsymbol{Q}_P^1$ (the sum of $-\nabla_h\cdot\boldsymbol{Q}_P^1$ and $-\nabla_z\cdot\boldsymbol{Q}_P^1$), together with the total TIW EKE (K^1). It can be seen that the seasonal variation of $-\nabla\cdot\boldsymbol{Q}_P^1$ exhibit simultaneously positive (negative) relations with the seasonal K^1 in SY (SubR). This strong spatial and seasonal correlation confirms that the nonlocal energy pathway fulfilled by pressure work is the major seasonal K^1 generation (damping) mechanism in SY (SubR). In SubR, the simultaneous correlation coefficients between the 15-year time series of $-\nabla_z\cdot\boldsymbol{Q}_P^1$ and $-\nabla_h\cdot\boldsymbol{Q}_P^1$, and K^1 are -0.89 and -0.82, respectively. In SR, the correlation coefficient between $-\nabla_h\cdot\boldsymbol{Q}_P^1$ and K^1 is -0.81. These results suggest that the strength of TIW EKE modulates the strength of the outward energy transportation.

In addition to the seasonal variation, the TIWs also vary on the interannual time scale (Contreras 2002), which can be readily seen in the standard error bars in Fig. 7. The envelope of K^1 is significantly wider in the high-level months (i.e., August-January) than the low-level months, suggesting that the TIWs exhibits strong interannual variability during their active season. We also find that the primary energy sources for K^1 in the four subdomains, i.e., $-\nabla_h\cdot\boldsymbol{Q}_P^1$ in SY, $-\nabla_z\cdot\boldsymbol{Q}_P^1$ and $\Gamma_K^{0\to1}$ in SR, $-b^1$ in SubY, and $\Gamma_K^{0\to1}$ and $-b^1$ in SubR, also undergo interannual modulations, especially during the high-level period (Fig. 7). Overall, the seasonal cycles of these dominant processes are statistically significant due to the relatively small standard errors, suggesting that our results are robust. The dynamics of TIW variability on the interannual time scale is certainly an interesting topic, which is beyond the scope of this study. Recently, Yang and Liang, 2019 found that the downscale canonical barotropic transfer determines the interannual modulation of the high-frequency EKE in the Equatorial Pacific, which tends to increase (decrease) during La Niña (El Niño) years.

5. Conclusions

Using the $(1/12.5)^\circ$ HYCOM reanalysis data, a recently developed functional apparatus, multiscale window transform (MWT), the MWT-based canonical transfer theory and localized multiscale energetics analysis have been employed to investigate the energy sources of the two distinct TIW modes in the equatorial Pacific, i.e., the Yanai- and Rossby-mode TIWs. MWT was first used to decompose the multiscale equatorial Pacific current system into three orthogonal temporal scale windows, namely, a background flow window (periods >48 days), a TIW window (periods of 12–48 days), and a high-frequency window (periods <12 days). Two latitude bands (2°S-1°N and 1–7°N) of high TIW-scale EKE levels are identified, which are respectively corresponding to the preferred regions for the development of the Yanai-mode and Rossby-mode TIWs as reported in previous studies (Halpern et al., 1988; Qiao and Weisberg 1995; Lyman et al., 2007). To further differentiate the vertical dynamics, we split the upper water column (0–200 m) into a surface layer (0–30 m) and a subsurface layer (30–200 m). To this end, four individual subdomains, i.e., the surface of the Yanai-mode region (SY), the subsurface of the Yanai-mode region (SubY), the surface of the Rossby-mode region (SR), and the subsurface of the Rossby-mode region (SubR) are introduced. The spatio-temporal variations of the TIW-scale energetics in each subdomain and the dynamical coupling between these subdomains are examined.

Although from a domain-integrated perspective, barotropic and baroclinic instabilities are the two major mechanisms in generating TIWs, as also shown in previous studies (e.g., Wang et al., 2017), the dominant factors controlling the TIW EKE in the four considered subdomains are quite different. In the subsurface layer, instability processes prevail: the barotropic instability pathway is the dominant EKE generation mechanism in SubY, while the baroclinic instability pathway dominates the EKE generation in SubR. In contrast, the nonlocal mechanism fulfilled by pressure work is prominent for the EKE generation in the surface layer. Southward and upward energy flux facilitated by pressure work transports the TIW EKE meridionally to the equator from the north and vertically to the surface from the subsurface layer. Upward energy flux mainly transports the TIW EKE from SubR to SR, and southward energy flux mainly transports the TIW EKE from SR and SubR to SY and SubY. As a result, horizontal (vertical) pressure work serves as a source of the TIW EKE in SY (SR), while pressure work is the dominant sink of the TIW EKE in SubR. The southward and upward pressure fluxes substantially couple the Yanai-mode and Rossby-mode TIWs, and the subsurface and surface layers, leading to the close relationship between the different layers and regions of TIWs. It is worth noting that the connection between the surface and subsurface layers of the Yanai-mode TIWs is weaker than that of the Rossby-mode TIWs due to the weaker vertical pressure flux between them. To our best knowledge, this nonlocal energy pathway has not been identified in previous studies. In addition, we find that the above energy pathway also holds for seasonal TIW evolutions. In all the four subdomains, the strength of TIW EKE reaches a minimum in spring and a maximum in autumn. The seasonal cycle of the TIW EKE in SY (SubR) is in a simultaneously positive (negative) correlation with the energy transport via pressure work.

Our results highlight the importance of nonlocal sources of the TIW EKE in the equatorial Pacific. Significant nonlocal energy transport is found to occur not only in the horizontal direction via meridional pressure flux as reported in previous studies (Luther and Johnson 1990; Masina et al., 1999), but also in the vertical direction through vertical pressure flux, which has been recently recognized as the dominant physical process in redistributing EKE among the ocean surface, interior, and deep layers in several ocean sectors, such as the North Atlantic (Zhai and Marshall 2013), Gulf of Mexico (Yang et al., 2020), Kuroshio Extension (Yang et al., 2021a), and South China Sea (Quan et al., 2022). This suggests that the nonlocality of eddy energy should be taken into account in eddy parameterization schemes in coarse-resolution climate models.

The three-scale window energetics framework also enables us to investigate the mutual interaction between the TIWs and higher-frequency variability. The energy cascade direction between these two processes is generally forward, indicating that the high-frequency fluctuations act to dampen the TIW variability. However, this forward cascade is an order of magnitude smaller in comparison to the dominant processes in the TIW-scale energetics and thus has limited influence on the TIWs. The present HYCOM reanalysis resolution only allows submesoscale features to be partially resolved, which could underestimate the influence of the high-frequency fluctuations on TIWs in this study

(Uchida et al., 2017). Indeed, using a high-resolution model, Marchesiello et al. (2011) have pointed out the important role played by submesoscale motions in restratifying the mixed layer in TIWs. We therefore look forward to extending this study to more detailed submesoscale processes with high-resolution models.

Declaration of competing interest

Data availability

Data will be made available on request.

Acknowledgments

Thanks are due to two anonymous referees for their valuable suggestions. WBH thanks Yuhui Zhao and Guanqi Fu for their suggestions and support. The HYCOM, AVISO, and TAO datasets are available, respectively, at the Asia-Pacific Data-Research Center (APDRC; http://apdrc.soest.hawaii.edu/dods/public_ofes/HYCOM/GLBv0.08/interpolated_daily_snapshot; download date: Nov. 11th, 2021), at the Copernicus Marine Environment Monitoring Service (CMEMS; https://data.marine.copernicus.eu/product/MULTIOBS_GLO_PHY_REP_015_004/download?dataset = dataset-uv-rep-daily; download date: Sep. 28th, 2021), and at the National Oceanic and Atmospheric Administration (NOAA; https://www.pmel.noaa.gov/tao/drupal/disdel/; download date: Jan. 9th, 2022). The MWT-based multiscale energetics analysis package can be downloaded at http://www.ncoads.cn/upload/202009/24/ms-eva_ocean.zip. This study is supported by National Science Foundation of China (NSFC) (Grants No. 42230105, 42276017, 41975064), by Southern Marine Science and Engineering Guangdong Laboratory (Zhuhai) through the Startup Foundation, by Shanghai B & R Joint Laboratory Project (Grant No. 22230750300), and by Shanghai International Science and Technology Partnership Project (Grant No. 21230780200). The support from the High Performance Computing Center at Nanjing University of Information Science and Technology is acknowledged.

References

An, S.-I., 2008. Interannual variations of the tropical ocean instability wave and ENSO. J. Clim. 21, 3680–3686. https://doi.org/10.1175/2008JCLI1701.1.

Ascani, F., Firing, E., McCreary, J.P., Brandt, P., Greatbatch, R.J., 2015. The deep equatorial ocean circulation in wind-forced numerical solutions. J. Phys. Oceanogr. 45, 1709–1734. https://doi.org/10.1175/JPO-D-14-0171.1.

Bryden, H.L., Brady, E.C., 1989. Eddy momentum and heat fluxes and their effects on the circulation of the equatorial Pacific Ocean. J. Mar. Res. 47, 55–79. https://doi.org/10.1357/002224089785076389.

Chelton, D.B., Coauthors, 2001. Observations of coupling between surface wind stress and sea surface temperature in the eastern tropical pacific. J. Clim. 14, 1479–1498. https://doi.org/10.1175/1520-0442(2001)014<1479:OOCBSW>2.0.CO;2.

Contreras, R.F., 2002. Long-term observations of tropical instability waves. J. Phys. Oceanogr. 32, 2715–2722. https://doi.org/10.1175/1520-0485(2002)032<2715:LTOOTI>2.0.CO;2.

Cox, M.D., 1980. Generation and propagation of 30-day waves in a numerical model of the pacific. J. Phys. Oceanogr. 10, 1168–1186. https://doi.org/10.1175/1520-0485(1980)010<1168:GAPODW>2.0.CO;2.

Cummings, J.A., Smedstad, O.M., 2013. In: Park, S.K., Xu, L. (Eds.), Variational Data Assimilation for the Global Ocean. *Data Assimilation For Atmospheric, Oceanic and Hydrologic Applications*, II. Springer Berlin Heidelberg, pp. 303–343.

Flament, P.J., Kennan, S.C., Knox, R.A., Niiler, P.P., Bernstein, R.L., 1996. The three-dimensional structure of an upper ocean vortex in the tropical Pacific Ocean. Nature 383, 610–613. https://doi.org/10.1038/383610a0.

Halpern, D., Knox, R.A., Luther, D.S., 1988. Observations of 20-day period meridional current oscillations in the upper ocean along the pacific equator. J. Phys. Oceanogr. 18, 1514–1534. https://doi.org/10.1175/1520-0485(1988)018<1514:OODPMC>2.0.CO;2.

Holmes, R.M., Thomas, L.N., 2016. Modulation of tropical instability wave intensity by equatorial kelvin waves. J. Phys. Oceanogr. 46, 2623–2643. https://doi.org/10.1175/JPO-D-16-0064.1.

Kennan, S.C., Flament, P.J., 2000. Observations of a tropical instability vortex. J. Phys. Oceanogr. 30, 2277–2301. https://doi.org/10.1175/1520-0485(2000)030<2277:OOATIV>2.0.CO;2.

Kimoto, M., Imada, Y., 2012. Parameterization of tropical instability waves and examination of their impact on ENSO characteristics. J. Clim. 25, 4568–4581. https://doi.org/10.1175/jcli-d-11-00233.1.

Körner, M., Claus, M., Brandt, P., Tuchen, F.P., 2022. Sources and pathways of intraseasonal meridional kinetic energy in the equatorial atlantic ocean. J. Phys. Oceanogr. 52, 2445–2462. https://doi.org/10.1175/JPO-D-21-0315.1.

Legeckis, R., 1977. Long waves in the eastern equatorial Pacific Ocean: a view from a geostationary satellite. Science 197, 1179–1181. https://doi.org/10.1126/science.197.4309.1179.

Liang, X.S., 2016. Canonical transfer and multiscale energetics for primitive and quasigeostrophic atmospheres. J. Atmos. Sci. 73, 4439–4468. https://doi.org/10.1175/JAS-D-16-0131.1.

Liang, X.S., Robinson, A.R., 2005. Localized multiscale energy and vorticity analysis: I. Fundamentals. Dynam. Atmos. Oceans 38, 195–230. https://doi.org/10.1016/j.dynatmoce.2004.12.004.

Liang, X.S., Anderson, D.G.M., 2007. Multiscale window transform. Multiscale Model. Simul. 6, 437–467. https://doi.org/10.1137/06066895X.

Liu, C., Fang, L., Köhl, A., Liu, Z., Smyth, W.D., Wang, F., 2019a. The subsurface mode tropical instability waves in the equatorial Pacific Ocean and their impacts on shear and mixing. Geophys. Res. Lett. 46, 12270–12278. https://doi.org/10.1029/2019gl085123.

Liu, C., Fang, L., Smyth, W.D., Wang, X., Köhl, A., Wang, F., Liu, Z., 2019b. The Northeast-Southwest oscillating equatorial mode of the tropical instability wave and its impact on equatorial mixing. Geophys. Res. Lett. 46, 218–225. https://doi.org/10.1029/2018gl080226.

Luther, D.S., Johnson, E.S., 1990. Eddy energetics in the upper equatorial pacific during the Hawaii-to-Tahiti shuttle experiment. J. Phys. Oceanogr. 20, 913–944. https://doi.org/10.1175/1520-0485(1990)020<0913:EEITUE>2.0.CO;2.

Lyman, J.M., Johnson, G.C., Kessler, W.S., 2007. Distinct 17- and 33-day tropical instability waves in subsurface observations. J. Phys. Oceanogr. 37, 855–872. https://doi.org/10.1175/jpo3023.1.

Marchesiello, P., Capet, X., Menkes, C., Kennan, S.C., 2011. Submesoscale dynamics in tropical instability waves. Ocean Model. 39, 31–46. https://doi.org/10.1016/j.ocemod.2011.04.011.

Martinez, E., Raapoto, H., Maes, C., Maamaatuaihutapu, K., 2018. Influence of tropical instability waves on phytoplankton biomass near the marquesas islands. Rem. Sens. 10, 640. https://doi.org/10.3390/rs10040640.

Masina, S., Philander, S.G.H., Bush, A.B.G., 1999. An analysis of tropical instability waves in a numerical model of the Pacific Ocean: 2. Generation and energetics of the waves. J. Geophys. Res.: Oceans 104, 29637–29661. https://doi.org/10.1029/1999jc900226.

McPhaden, M.J., 1995. The tropical atmosphere ocean array is completed. Bull. Am. Meteorol. Soc. 76, 739–744. https://doi.org/10.1175/1520-0477-76.5.739.

Oort, A.H., Ascher, S.C., Levitus, S., Peixóto, J.P., 1989. New estimates of the available potential energy in the world ocean. J. Geophys. Res. 94, 3187. https://doi.org/10.1029/JC094iC03p03187.

Pedlosky, J., 1979. Geophysical Fluid Dynamics. Springer US, p. 1007.

Pezzi, L.P., Vialard, J., Richards, K.J., Menkes, C., Anderson, D., 2004. Influence of ocean-atmosphere coupling on the properties of tropical instability waves. Geophys. Res. Lett. 31 https://doi.org/10.1029/2004GL019995.

Philander, S.G.H., 1976. Instabilities of zonal equatorial currents. J. Geophys. Res. 81, 3725–3735. https://doi.org/10.1029/JC081i021p03725.

Philander, S.G.H., 1978. Instabilities of zonal equatorial currents, 2. J. Geophys. Res. 83 https://doi.org/10.1029/JC083iC07p03679.

Qiao, L., Weisberg, R.H., 1995. Tropical instability wave kinematics: observations from the tropical instability wave experiment. J. Geophys. Res.: Oceans 100, 8677–8693. https://doi.org/10.1029/95JC00305.

Qiao, L., Weisberg, R.H., 1998. Tropical instability wave energetics: observations from the tropical instability wave experiment. J. Phys. Oceanogr. 28, 345–360. https://doi.org/10.1175/1520-0485(1998)028<0345:TIWEOF>2.0.CO;2.

Quan, Q., Liu, Z., Yang, Y., Cai, Z., Zhang, H., Liu, X., 2022. Characterization of intraseasonal fluctuations in the abyssal South China Sea: an insight into the energy pathway. Prog. Oceanogr. https://doi.org/10.1016/j.pocean.2022.102829.

Seo, H., Jochum, M., Murtugudde, R., Miller, A.J., Roads, J.O., 2007. Feedback of tropical instability-wave-induced atmospheric variability onto the ocean. J. Clim. 20, 5842–5855. https://doi.org/10.1175/JCLI4330.1.

Specht, M.S., Jungclaus, J., Bader, J., 2021. Identifying and characterizing subsurface tropical instability waves in the atlantic ocean in simulations and observations. J. Geophys. Res.: Oceans 126. https://doi.org/10.1029/2020JC017013.

Traon, P.Y.L., Nadal, F., Ducet, N., 1998. An improved mapping method of multisatellite altimeter data. J. Atmos. Ocean. Technol. 15, 522–534. https://doi.org/10.1175/1520-0426(1998)015<0522:AIMMOM>2.0.CO;2.

Tuchen, F.P., Brandt, P., Claus, M., Hummels, R., 2018. Deep intraseasonal variability in the central equatorial atlantic. J. Phys. Oceanogr. 48, 2851–2865. https://doi.org/10.1175/JPO-D-18-0059.1.

Uchida, T., Abernathey, R., Smith, S., 2017. Seasonality of eddy kinetic energy in an eddy permitting global climate model. Ocean Model. 118, 41–58. https://doi.org/10.1016/j.ocemod.2017.08.006.

Vialard, J., Menkes, C., Boulanger, J.-P., Delecluse, P., Guilyardi, E., McPhaden, M.J., Madec, G., 2001. A model study of oceanic mechanisms affecting equatorial pacific sea surface temperature during the 1997–98 El Niño. J. Phys. Oceanogr. 31, 1649–1675. https://doi.org/10.1175/1520-0485(2001)031<1649:AMSOOM>2.0.CO;2.

Wang, M., Du, Y., Qiu, B., Cheng, X., Luo, Y., Chen, X., Feng, M., 2017. Mechanism of seasonal eddy kinetic energy variability in the eastern equatorial Pacific Ocean. J. Geophys. Res. Oceans 122, 3240–3252. https://doi.org/10.1002/2017JC012711.

Wang, M., Du, Y., Qiu, B., Cheng, X., Luo, Y., Chen, X., Xie, S.-P., Feng, M., 2019. Dynamics on seasonal variability of EKE associated with TIWs in the eastern equatorial Pacific Ocean. J. Phys. Oceanogr. 49, 1503–1519. https://doi.org/10.1175/jpo-d-18-0163.1.

Wang, M., Qiu, B., Cheng, X., Luo, Y., Chen, X., Feng, M., Xie, S.-P., Shen, S.S.P., Du, Y., 2020. Rossby and Yanai modes of tropical instability waves in the equatorial Pacific Ocean and a diagnostic model for surface currents. J. Phys. Oceanogr. 50, 3009–3024. https://doi.org/10.1175/jpo-d-20-0063.1.

Weisberg, R.H., Weingartner, T.J., 1988. Instability waves in the equatorial atlantic ocean. J. Phys. Oceanogr. 18, 1641–1657. https://doi.org/10.1175/1520-0485(1988)018<1641:IWITEA>2.0.CO;2.

Wyrtki, K., 1978. Lateral oscillations of the pacific equatorial countercurrent. J. Phys. Oceanogr. 8, 530–532. https://doi.org/10.1175/1520-0485(1978)008<0530:LOOTPE>2.0.CO;2.

Xu, F., Liang, X.S., 2020. The synchronization between the zonal jet stream and temperature anomalies leads to an extremely freezing north America in january 2019. Geophys. Res. Lett. 47 https://doi.org/10.1029/2020GL089689.

Xue, A., Jin, F.-F., Zhang, W., Boucharel, J., Zhao, S., Yuan, X., 2020. Delineating the seasonally modulated nonlinear feedback onto ENSO from tropical instability waves. Geophys. Res. Lett. 47 https://doi.org/10.1029/2019gl085863.

Yang, Y., Liang, X.S., 2019. Spatiotemporal Variability of the Global Ocean Internal Processes Inferred from Satellite Observations. J. Phys. Oceanogr. 49, 2147–2164. https://doi.org/10.1175/JPO-D-18-0273.1.

Yang, Y., Weisberg, R.H., Liu, Y., Liang, X.S., 2020. Instabilities and multiscale interactions underlying the loop current eddy shedding in the Gulf of Mexico. J. Phys. Oceanogr. 50, 1289–1317. https://doi.org/10.1175/JPO-D-19-0202.1.

Yang, Y., Weisberg, R.H., Liu, Y., Liang, X.S., Sasaki, H., 2021a. Vertical coupling and dynamical source for the intraseasonal variability in the deep Kuroshio Extension. Ocean Dynam. 71, 1069–1086. https://doi.org/10.1007/s10236-021-01482-9.

Yang, Y., Weisberg, R.H., Liu, Y., Liang, X.S., Sasaki, H., McWilliams, J.C., San Liang, X., Zhang, H., Weisberg, R.H., Liu, Y., Menemenlis, D., 2021b. Spatial and temporal characteristics of the submesoscale energetics in the Gulf of Mexico. J. Phys. Oceanogr. 51, 475–489. https://doi.org/10.1175/JPO-D-20-0247.1.

Yu, Z., McCreary, J.P., Proehl, J.A., 1995. Meridional asymmetry and energetics of tropical instability waves. J. Phys. Oceanogr. 25, 2997–3007. https://doi.org/10.1175/1520-0485(1995)025<2997:MAAEOT>2.0.CO;2.

Zhai, X., Marshall, D.P., 2013. Vertical eddy energy fluxes in the North atlantic subtropical and subpolar gyres. J. Phys. Oceanogr. 43, 95–103. https://doi.org/10.1175/JPO-D-12-021.1.

Zhang, R.-H., 2014. Effects of tropical instability wave (TIW)-induced surface wind feedback in the tropical Pacific Ocean. Clim. Dynam. 42, 467–485. https://doi.org/10.1007/s00382-013-1878-6.

Zhang, Z., Liang, X.S., 2021. Multiscale interactive processes underlying the heavy rainstorm associated with a landfalling atmospheric river. Atmosphere 13, 29. https://doi.org/10.3390/atmos13010029.

Zhao, Y., Yang, Y., Liang, X.S., Zhang, Y., 2022. Different mechanisms for the seasonal variations of the mesoscale eddy energy in the South China Sea. Deep Sea Res. Oceanogr. Res. Pap. 179, 103677 https://doi.org/10.1016/j.dsr.2021.103677.